remote sensing

MDPI

*Article*

# A Multivariable Study of a Traveling Ionosphere Disturbance Using the Arecibo Incoherent Scatter Radar

**Qihou Zhou [1,*], Yanlin Li [1] and Yun Gong [2]**

[1] Department of Electrical and Computer Engineering, Miami University, Oxford, OH 45056, USA; liy27@miamioh.edu
[2] School of Electronic Information, Wuhan University, Wuhan 430072, China
* Correspondence: zhouq@miamioh.edu

**Abstract:** We present the first simultaneous observations of a traveling ionosphere wave (TID) event, measuring electron concentration ($N_e$), vertical plasma drift ($V_z$), and ion and electron temperatures ($T_i$, $T_e$) using the Arecibo incoherent scatter radar. A TID with a period of 135 min was evident in all four state variables in the thermosphere. The amplitudes of $V_z$ and relative $T_i$ fluctuations show only small height variations from 200 to 500 km and their vertical wavelengths increase with altitude. The $T_e$ fluctuation shows different characteristics from EISCAT in both phase and amplitude. When the geomagnetic dip angle is 45°, half of the driving gravity wave's (GW's) equatorward velocity is mapped to $V_z$. This meridional-to-vertical velocity coupling amplifies GW's effect in $N_e$ through vertical transport. The amplifying and anisotropic effects of the geomagnetic field explain the ubiquitous presence of TIDs and their preferred equatorward propagation direction in the geomagnetic mid-latitudes, as well as the midnight collapse phenomenon observed at Arecibo.

**Keywords:** mid-latitude ionosphere; traveling ionosphere disturbance; thermospheric gravity wave; Arecibo ISR

check for updates

**Citation:** Zhou, Q.; Li, Y.; Gong, Y. A Multivariable Study of a Traveling Ionosphere Disturbance Using the Arecibo Incoherent Scatter Radar. *Remote Sens.* **2024**, *16*, 4104. https://doi.org/10.3390/rs16214104

Academic Editor: Roberto Orosei

Received: 31 August 2024
Revised: 24 October 2024
Accepted: 31 October 2024
Published: 2 November 2024

## 1. Introduction

Thermospheric gravity waves (GWs) and traveling ionosphere disturbances (TIDs) are global phenomena that have been widely observed by various radar/radio and optical methods (e.g., [1–4]). Large-scale TIDs originate in the auroral zone caused by intense Joule heating and auroral particle precipitation associated with geomagnetic storms [5]. It is well-documented that GWs induce wave-like perturbations in ionosphere state variables. The ubiquitous presence of wave-like events has been established through electron density observations by the Arecibo incoherent scatter radar (ISR) (e.g., [6,7]). Although the sensitivity of Arecibo ISR spans from the D- to the F-region (e.g., [8–10]), TID observations have been confined to electron densities above 125 km so far. Here, we report the first simultaneous observations of TIDs, measuring electron concentration ($N_e$), vertical ion velocity ($V_z$), and electron and ion temperatures ($T_e$, $T_i$) at Arecibo using a new ISR analysis method reported in [11]. Other multivariable TID studies were carried out at high latitudes using the EISCAT radar ([1,12]).

Numerous theoretical and modeling studies have focused on thermospheric gravity waves (GWs), which are characterized by strong dissipation due to large molecular viscosity, thermal diffusion, and ion drag (e.g., see [13–16], and references therein). While the governing equations for GWs are largely the same across all theories, the underlying assumptions can significantly affect the conclusions. Full-wave models (FWMs), applicable for steady-state sources, indicate that the vertical wavelength increases with altitude (e.g., [17,18]). The wave-packet model (WPM), which applies to time-dependent and localized sources, shows that the vertical wavelength remains the same or decreases above the maximum dissipation height (e.g., [19]). Thus, observing the vertical wavelength is particularly important when determining which type of model more suitably describes the propagation of GWs and TIDs.

In the following section, we present the observational results of $N_e$, $V_z$, $T_i$, and $T_e$, with emphasis on their perturbations. In Section 3, we discuss the amplitude, phase, and vertical wavelength of the TID as revealed in the four ionosphere state variables. We further discuss the coupling between TID and GW. The main results and conclusions are summarized in Section 4.

## 2. Data Analysis and Results

The data used for this study were taken by the Arecibo ISR (18.3°N, 66.7°W; dip angle: 43.6°) located in Puerto Rico on 12 September 2014, using the coded-long-pulse program. Interference mitigation and data reduction from raw voltage samples to geophysical parameters, including the molecular ion fraction using a new fitting method, are discussed in [11,20]. In Figure 1, we present the plasma frequency (which is proportional to the square root of the electron density), upward ion drift velocity ($V_z$), and electron and ion temperatures ($T_e$, $T_i$) for 12 September 2014. Although data on the molecular ion fraction are available, they do not have the time resolution and altitude coverage for TID studies. The independent time and height resolution values are 15 min and 18 km, respectively. The minimum $f_of_2$ (plasma frequency at the F-region peak height), occurring at 7:00 LT and 250 km, corresponds to a divergence region (i.e., ions move upward above this point and downward below it), and the maximum $f_of_2$ (occurring at around 300 km and 16:00 LT) corresponds to a convergence region (i.e., ions move upward below this altitude and downward above it) as seen in the velocity plot. Such behaviors indicate that the short-term variations in F-region electron density are controlled by vertical transport. The largest electron temperature elevation over ion temperature (as measured by $T_e/T_i$) after 8:00 LT occurs slightly below the peak altitude of the electron concentration ($h_mf_2$) due to the high photoionization rate. The electron temperature shows an anticorrelation with electron concentration above 200 km. While the simultaneous observations of state variables reveal the fundamental principles of aeronomy, our focus here is on the study of TIDs.

To reveal perturbations in the state variables, we smooth the data using a time window of 135 minutes and a height window of 18 km. The averaged data are subtracted from the data shown in Figure 1 to obtain fluctuations for each variable. To compress the dynamic range, we use the signed square root of the absolute value (SSA) function, defined as $F_{\text{ssa}}(x) = \begin{cases} \sqrt{x}, & x \geq 0 \\ -\sqrt{|x|}, & x < 0 \end{cases}$. We use $\Delta x$ and $\Delta x/x$ to indicate the fluctuation and relative fluctuation of variable $x$, respectively. The SSAs of $\Delta N_e/N_e$, $\Delta T_e/T_e$, $\Delta T_i/T_i$, and $\Delta V_z$ as functions of altitude and time are plotted in Figure 2. $\Delta N_e/N_e$ is similar to what was previously reported at Arecibo ([7,10,21]). The wave structures in $V_z$, $T_i$, and $T_e$ have not been reported at middle or low latitudes. On a one-hour time scale, the peak trough variation of $\Delta N_e/N_e$ often exceeds 100% above 200 km, while it is much smaller than 180 km. Below 200 km, $\Delta N_e/N_e$ and $\Delta T_e/T_e$ exhibit smaller amplitudes and different characteristics than those above. As there is no substantial change in the amplitude of the vertical velocity perturbation, the larger amplitude variations at higher altitudes in $\Delta N_e/N_e$ and $\Delta T_e/T_e$ are mainly due to the change in ion composition from dominantly molecular ions below 170 km to primarily $O^+$ above 200 km in the F-region ([11]). In the region where $O^+$ dominates, the largest $\Delta N_e/N_e$ occurs slightly below $h_mf_2$, the peak altitude of the F2 region. $N_e$ and $T_e$ are closely coupled through the energy balance equation. The anticorrelation between $N_e$ and $T_e$ discussed in [22], above 180 km, is seen here as well. The $\Delta T_i/T_i$ perturbation is larger below 200 km than above, with the largest amplitude occurring between 9:00 and 10:00 LT, in conjunction with the largest changes in ion velocity in both temporal and spatial directions.

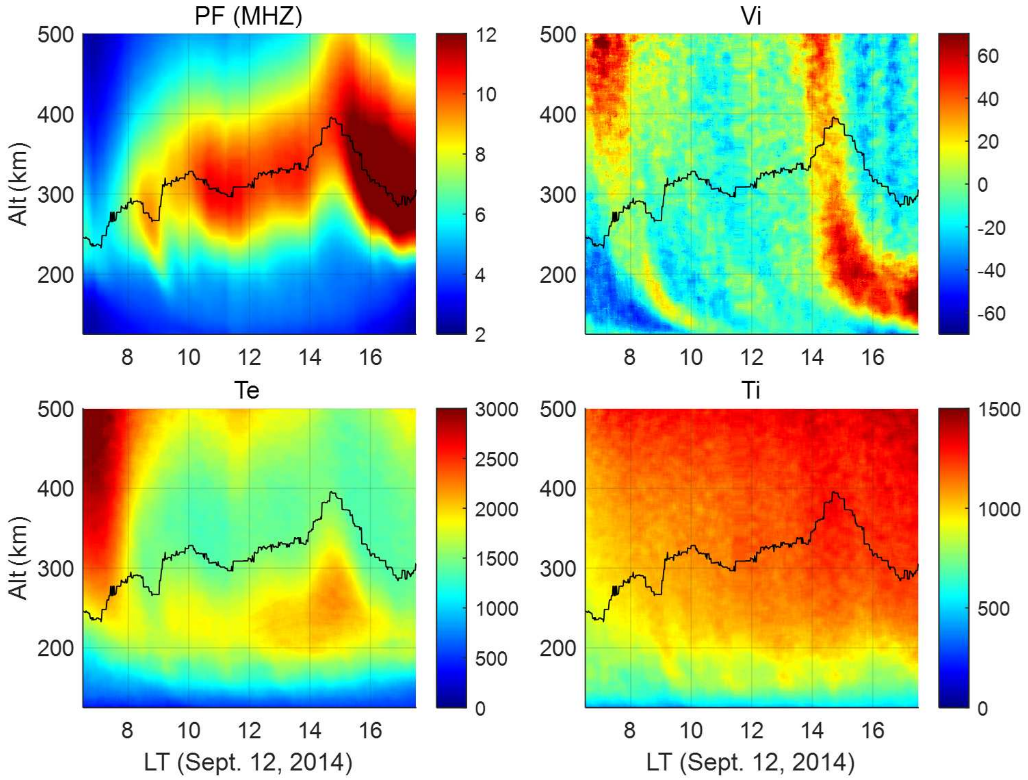

**Figure 1.** (**a**) Plasma frequency (MHz); (**b**) upward vertical ion velocity (m/s); (**c**) electron temperature (K); (**d**) ion temperature (K) measured by the Arecibo ISR on 12 September 2014. The superposed black line is $h_m f_2$.

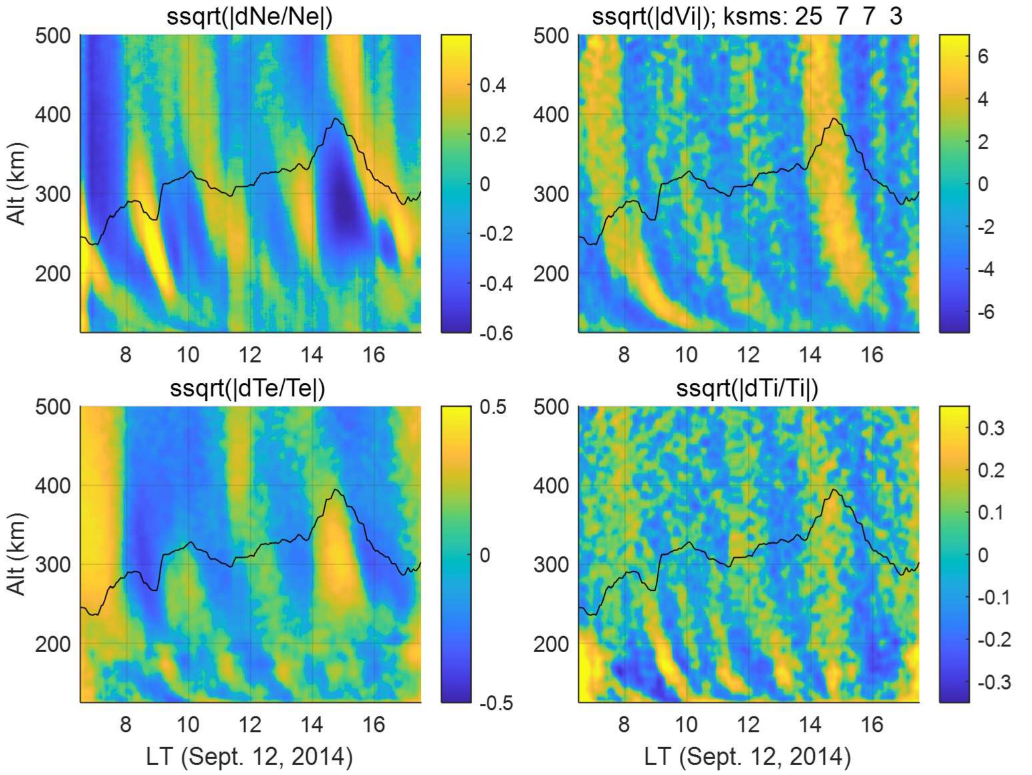

**Figure 2.** Fluctuations of (**a**) $\Delta N_e/N_e$, (**b**) $\Delta T_e/T_e$, (**c**) $\Delta T_i/T_i$, (**d**) $\Delta V_z$ for the data displayed on 12 September 2014. The displayed values are transformed using the signed square root method. The data are obtained by subtracting a 2D moving average from the data shown in Figure 1.

To analyze the frequency components, we display the magnitudes of the Fourier transform of the perturbations between 8:00 and 17:00 LT in Figure 3. The values at a period of 135 min, corresponding to the frequency of 0.0074/min, are scaled to represent the fitting amplitude of a sinusoidal wave. For the most part, the main frequency components of $\Delta T_i/T_i$ and $\Delta V_z$ are confined between 108 and 180 min (0.0056–0.0093/min in frequency), while $\Delta N_e/N_e$ and $\Delta T_e/T_e$ have significant low-frequency components. Below 200 km, the dominant frequency for $\Delta V_z$ is at 180 min, while $\Delta T_e/T_e$ and $\Delta T_i/T_i$ have similar frequencies at 108 min. In Figure 4a, we plot the "bandpass amplitude" of the fluctuations for periods from 108 to 180 min. This "bandpass amplitude" is the square root of the total power spectral densities within the period from 108 to 180 min. For this discussion, we will use $A(x)$ to represent the bandpass amplitude for variable $x$. $A(x)$ is a proxy for the amplitude of the TID observed in variable $x$. As shown in Figure 4a, at 300 km, $A(\Delta N_e/N_e)$ is the largest, which is slightly below the average, $h_m f_2$, with an amplitude of 16%. Above 300 km, $A(\Delta T_e/T_e)$ is about half of $A(\Delta N_e/N_e)$, and it decreases very quickly with decreasing altitude below 300 km. Below 230 km, $A(\Delta T_i/T_i)$ is about the same as $A(\Delta T_e/T_e)$ and much smaller than $A(\Delta T_e/T_e)$ in the main F2 region from 250 to 400 km. $A(\Delta V_z)$, at about 10 m/s, and $A(\Delta T_i/T_i)$, exhibit small altitudinal variations from 200 to 500 km.

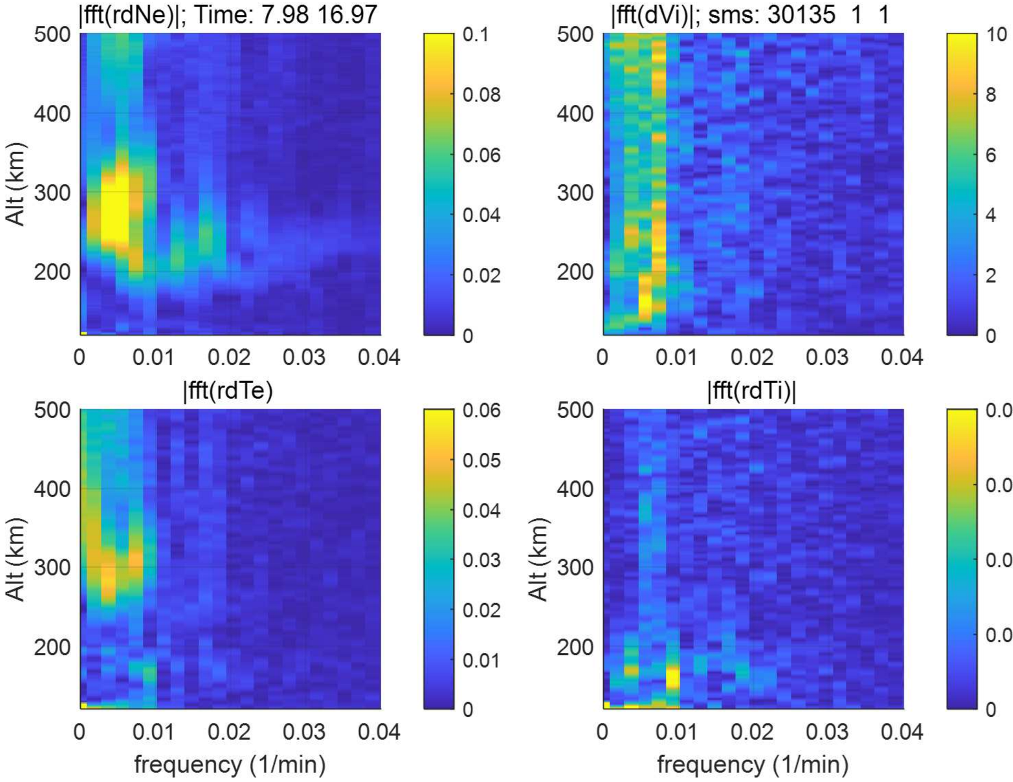

**Figure 3.** Magnitude of the Fourier transform for the data shown in Figure 2. The frequency resolution is 0.0019/min.

To explore the TID phase relationships in the four state variables, we plot their phase angles (in cycles) at the period of 135 min in Figure 4b. For easier comparison, the phase angle of $-\Delta N_e/N_e$, $\phi(-\Delta N_e/N_e)$, is plotted. The decreasing phase angle as a function of altitude indicates a downward phase progression. The rate of change of the phases in all four state variables is faster at lower altitudes than at higher ones. To quantitatively describe the phase angle, we model it using a 4-parameter exponential function, as $\phi(x;z) = a + be^{-\frac{(z-z_0)}{(h_0+\beta(z-z_0))^{1/2}}}$, for variable $x$ at altitude $z$ (in km), where $z_0$ is 149.70 km. Table 1 lists the fitting parameters of the four state variables. A large $h_0$, as observed for $N_e$, indicates a closer match to the linear phase. Because $z$ is common for all variables, we will shorten $\phi(x;z)$ as $\phi(x)$. The fitted $\phi(\Delta V_z)$ and $\phi(\Delta T_i/T_i)$ are plotted twice with a full cycle offset for easier comparison. The line size in Figure 4b is proportional to the relative magnitude of the Fourier transform (normalized by the maximum at the period of 135 min) shown in Figure 3. The altitudinal derivative of the phase is proportional to the vertical wavelength. We use $\lambda_z$ to denote the vertical wavelength and $\lambda_z(x)$ to denote the $\lambda_z$ for variable $x$. Using the fitted phases, $\lambda_z$ values for all four variables are shown in Figure 4c on a logarithm scale. For all four state variables, the overall trend is that $\lambda_z$ increases with altitude even though $\lambda_z(\Delta N_e/N_e)$ and $\lambda_z(\Delta T_e/T_e)$ appear to change from very large between 250 and 300 km to about 500 km above 350 km.

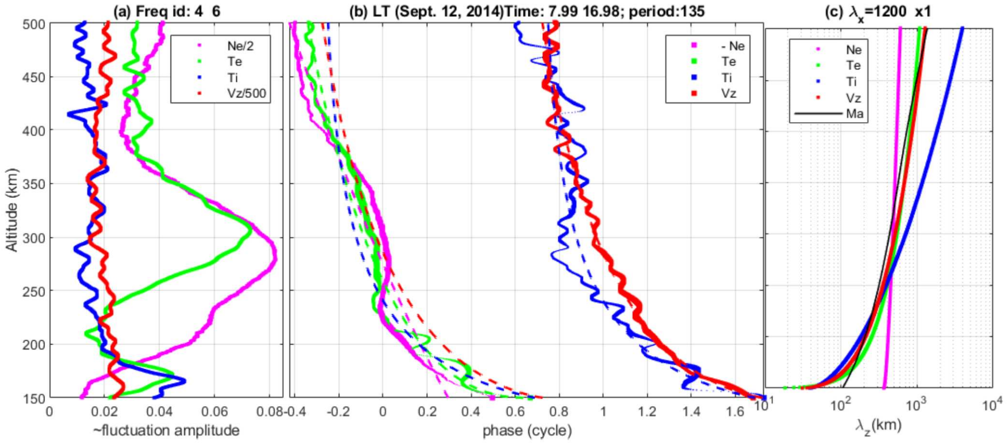

**Figure 4.** (**a**) Bandpass amplitudes of $0.5\Delta N_e/N_e$, $\Delta T_e/T_e$, $\Delta T_i/T_i$, and $\Delta V_z/500$. (**b**) Phase angles of $-\Delta N_e/N_e$, $\Delta T_e/T_e$, $\Delta T_i/T_i$, and $V_z$ on 12 September 2014, for the TID at 135 min. The thin lines denote the model-fitting results for the variable with the matching color. (**c**) Vertical wavelengths derived from the fitted phases in (**b**). The black line denotes the vertical wavelength derived from the dispersion relation in [23] with a horizontal wavelength of 1200 km and an intrinsic period of 135 min.

Figure 4b shows that $N_e$ is out of phase with $T_e$, i.e., $\phi(\Delta T_e/T_e) = \phi(-\Delta N_e/N_e) = \pi - \phi(\Delta N_e/N_e)$ in the entire altitude range of 200 to 500 km, which is common in ISR observations [22]. $\phi(\Delta T_e/T_e)$ and $\phi(\Delta T_i/T_i)$ are largely the same below 370 km. Above 350 km, $\phi(\Delta V_z)$ and $\phi(\Delta T_i/T_i)$ are about the same, with both showing little altitudinal variation. Among the four variables, $\phi(\Delta V_z)$ exhibits the smoothest variation across all altitudes. $\phi(\Delta T_i/T_i)$ departs from the exponential fitting the most at 280 km. On average, $\phi(\Delta V_z)$ is slightly larger than the three other phases, i.e., it lags slightly behind the others.

The TID event on 12 September was likely impacted by the geomagnetic storm ($K_p = 7$, $Dst_{\min} = -75$ nT) associated with a halo CME and an X1.6 flare that occurred on 10 September 2014. Details of the storm, including solar wind data from the ACE spacecraft and Dst observations, can be found in [24]. The max 3-hr kp index reached 7 from 12 to 15 UTC (8 to 11 LT); the kp variation can be found at https://www.spaceweatherlive.com/en/archive/2024/09/12/kp.html. We also note that the two bright yellow color bands in Figure 2 are separated by eight hours. The terdiurnal tide was previously found to be enhanced during a stratospheric warming event [25]. It is possible that the 8-hour tide and the 2-hour wave were enhanced due to the geomagnetic storm.

**Table 1.** Fitting parameters for the phases.

| | $a$ | $b$ | $h_0$ | $\beta$ |
|---|---|---|---|---|
| $-N_e$ | −2.683 | 2.979 | 1085 | 9.597 |
| $T_e$ | −1.190 | 1.828 | −1.3 | 24.45 |
| $T_i$ | −0.293 | 0.984 | 36.25 | 4.041 |
| $V_z$ | −0.647 | 1.373 | 35.6 | 12.41 |

## 3. Discussion

There is little doubt that the TID discussed here is generated by the GW. How the GW manifests in ionosphere variables depends on the coupling mechanisms between the neutral and ion variables. The couplings between $\Delta N_e/N_e$ and GW have been discussed by several authors (e.g., [21,26]). Ref. [12] provides a comprehensive discussion of the relationship between the various TID variables and GW. Our discussion here focuses on the effect of the geomagnetic dip angle on the coupling in the velocity between TID and GW and the subsequent impact on TID in other ionosphere variables.

In the F-region of the ionosphere, the ion velocity perpendicular to the geomagnetic field, $B$, is given by $\mathbf{E} \times \mathbf{B}/B^2$, where $B$ denotes the magnitude of $\mathbf{B}$. For convenience, the geomagnetic coordinate system is used. Accounting for the effect of the vertical neutral wind, but neglecting the field-aligned current, the ion velocity along $B$ (upward being positive) is as follows:

$$v_{Bu} = u_{\mathrm{eq}} \cos I + u_z \sin I - v_d \tag{1}$$

where $u_{\mathrm{eq}}$ and $u_z$ denote the equatorward and upward neutral winds, respectively, and $I$ denotes the dip angle. $v_d$ denotes the ambipolar diffusion velocity, whose expression can be found in [12,27]. Accounting for the effect of the electric field perpendicular to the field line, the theoretical upward ion vertical velocity, $v_z$, can be expressed as follows:

$$v_z = \frac{E_{ea}}{B^2} \cos I + \frac{\sin(2I)}{2} u_{\mathrm{eq}} + u_z \sin^2 I - v_d \sin I \tag{2}$$

where $E_{ea}$ denotes the eastward electric field. For $I = 45°$, applicable to Arecibo, the theoretical upward ion velocity perturbation can be expressed as follows:

$$\Delta v_z = \frac{\sqrt{2}\Delta E_{ea}}{2B^2} + \frac{1}{2}(\Delta u_{\mathrm{eq}} + \Delta u_z) - \frac{\sqrt{2}}{2}\Delta v_d \tag{3}$$

Diffusion is a response to the gradient and always works to reduce it. Its effect is secondary, as shown in [12]. Although $E_{ea}$ does not vary along the field line, it has a vertical variation because of the different field lines. $E_{ea}$ is generated through the dynamo effect mainly by the E-region's meridional wind. Due to the short vertical wavelength in the E-region and the integrated dynamo effect, $\Delta E_{ea}$ is not expected to be a significant part of $\Delta v_z$ most of the time. For $I = 45°$, we have the simplified expression of the following:

$$\Delta v_z \approx \frac{1}{2}(\Delta u_{\mathrm{eq}} + \Delta u_z) \tag{4}$$

The horizontal wind or its perturbation is expected to be much larger than that in the vertical direction. The large amplitude of a GW's horizontal wind perturbation is reflected in the vertical ion motion, which the radar can measure more accurately. The dependence of $\Delta v_z$ on the dip angle explains why TIDs are more easily observed at middle latitudes but more difficult above the equator. Equations (3) and (4) apply to all frequency components in the neutral wind. The effective conversion of meridional wind into vertical ion drift within the tidal components explains why dramatic changes $h_m f_2$ and $f_o f_2$, known as "midnight collapse", are often observed at Arecibo (e.g., [27]). Equation (1) shows that a vertically propagating GW above the equator cannot be detected from vertical ion motion no matter how large its amplitude is. Since $\Delta v_z$ is a linear combination of $\Delta u_{\mathrm{eq}}$ and $\Delta u_z$, its amplitude is linearly proportional to the amplitude of the GW, and it has the GW's vertical wavelength.

For mid-latitudes, Equation (3) shows that it is easiest to observe GWs whose horizontal velocities are aligned with the geomagnetic meridional plane. The classical polarization relationship for GWs in a non-dissipative atmosphere is expressed as $\Delta u_h \sim -\frac{k_z}{k_h}\Delta u_z$ ($\Delta u_h$ and $k_h$ denote the horizontal velocity perturbation and wavenumber, respectively), indicating that the upward velocity is in phase with the horizontal velocity in the direction of wave propagation for upward-propagating GWs (i.e., negative $k_z$). While the simplified polarization is likely modified by the presence of dissipations, Ref. [15] shows that the phase relationship between vertical and horizontal velocities still holds, at least under the assumption where $k_z^2 \gg k_h^2$ and $k_z^2 \gg \frac{1}{4H^2}$, with $H$ denoting the scale height. Equation (3) implies that the amplitude of an equatorward-propagating GW is larger than that of a poleward-propagating GW with the same perturbation amplitude. This is consistent with the preferred southward GW propagation directions observed at Arecibo [10] and by the MU radar in Japan, where $I = 42^\circ$ and the declination angle is 1° toward the east [3]. The slight southeastward tilt at Arecibo may also be influenced by the 8.5° declination of the geomagnetic field toward the west. In the polar region, TID and GW are expected to have the same anisotropic characteristics as $\Delta u_z \approx \Delta v_z$ when $I = 90^\circ$.

Due to the ionosphere's vertical stratification, vertical ion velocity perturbation amplifies the effect of TIDs on other state variables. The peak-to-trough perturbation of $\Delta N_e/N_e$ exceeds 100% in one hour, as seen in Figure 2. Such a large fluctuation overwhelms the GW-induced $N_e$ variations associated with density changes in neutral species, with $\Delta N_e/N_e$ being almost entirely attributable to the transport effect of $\Delta v_z$. The much smaller fluctuation amplitude below 180 km is due to the presence of large amounts of molecular ions whose short lifetime reduces the effect of transport.

The electron temperature variation is related to the electron density variation. As previously observed at Arecibo and EISCAT [22,28], Figure 4a shows that $\Delta N_e/N_e$ and $\Delta T_e/T_e$ are largely 180° out of phase. This is generally understood to be due to the cooling rate increasing faster than the heating rate as $N_e$ increases. A detailed analysis of the perturbation in [12] shows that $\Delta T_e/T_e$ is in phase with $\Delta T_i/T_i$ in the lower F-region, in anti-phase with $N_e$ in the main F-region, and in phase with $\Delta v_Z$ in the upper F-region. Our observation is consistent with this conclusion. Furthermore, our results indicate that all the phases of $\Delta V_z$, $\Delta T_i/T_i$, $\Delta T_e/T_e$, and $-\Delta N_e/N_e$ are within about 36° from 200 km to 500 km, with the phase of $\Delta V_z$ being slightly behind.

It is of interest to compare our results with those obtained from the EISCAT radar reported in [28]. The large dip angle of 77.6° at EISCAT results in 21% of the meridional wind being mapped as vertical ion velocity, compared to 50% at Arecibo. On average, we expect the vertical ion velocity perturbation at Arecibo to be larger than that at EISCAT, which is reflected in the ubiquitous presence of TID at Arecibo. The average ion velocity perturbation reported in [28] is about 4 m/s while ours is about 10 m/s. Since $V_z$ denotes the driving forces of the fluctuations of $N_e$ and $T_e$, $\Delta N_e/N_e$ and $\Delta T_e/T_e$ are also expected to be larger at Arecibo. The largest $\Delta N_e/N_e$ and $\Delta T_e/T_e$ near the F-region peak in our observations are 16% and 7%, respectively, while they are 5% and 1.5% at EISCAT, respectively. Of the four state variables, $\Delta T_e/T_e$ at the two sites displays the most distinct characteristics. The altitudinal variation of $\Delta T_e/T_e$ at Arecibo has a bell shape, with the maximum occurring near $h_m f_2$, while the EISCAT $\Delta T_e/T_e$ variation is small across the entire thermosphere and is largely flat above 300 km. The vertical wavelength of $\Delta T_e/T_e$ at EISCAT is larger than those of other state variables below 350 km, which is not the case at Arecibo. $\Delta T_i/T_i$ at Arecibo is only slightly larger than that at EISCAT. The closer match in $\Delta T_i/T_i$ at the two sites may indicate that this parameter is more closely coupled to the driving GW's temperature perturbation than with the $V_z$. While the comparison shows interesting similarities and differences, more observations are needed at Arecibo to confirm their generality. As mentioned in the introduction, the characteristics of the GW's vertical wavelength are considered critical when determining the applicability of theoretical GW models. The event discussed here and the EISCAT results from [28] show that the vertical wavelength increases with altitude, which can be interpreted as supporting the applicability of the full-wave model (FWM). Ref. [19] drew the opposite conclusion about the behavior of vertical wavelengths, drawing on results from the Poker Flat [29] and Arecibo ISRs. The cited Arecibo results were from the $N_e$ observations in [21] and a manuscript that was then in preparation, which appears to be [10].

Ref. [10] presented two sets of vertical wavelengths using $\Delta N_e/N_e$ data from 23 to 25 July 2009, from 130 km to 350 km. The first set of vertical wavelengths, $\lambda_z(\Delta N_e/N_e)$, is directly from $\Delta N_e/N_e$, and the second set, $\lambda_z(\Delta v_{Ne})$, is from the calculated ion velocities using $\Delta N_e/N_e$. $\lambda_z(\Delta N_e/N_e)$ and $\lambda_z(\Delta v_{Ne})$ are further divided into two groups, one for mostly morning hours and another for afternoon hours. While the morning $\lambda_z(\Delta N_e/N_e)$ appears to be flat from 250 km to 350 km, the afternoon $\lambda_z(\Delta N_e/N_e)$ appears to increase with altitude, even though the rate of increase is not large. We also note that the 350 km top altitude used in [10,21] makes it difficult to distinguish between a straight line and exponential growth when the vertical wavelength is much larger than the altitude range used for its derivation. $\lambda_z(\Delta v_{Ne})$ clearly decreases from 250 km to 350 km. The process of deriving $\lambda_z(\Delta v_{Ne})$, however, involves several assumptions, and the results contain several GW and ionosphere parameters, which may not be accurately measured. As deriving $\lambda_z(\Delta v_{Ne})$ is a highly involved process, its reliability is questionable. Any derived vertical wavelength variation needs to withstand visual tests. The vertical wavelength can be roughly seen from the contours of perturbation plots directly. Visual inspections of the published Arecibo $\Delta N_e/N_e$ plots (e.g., [7,10,21]) and Figure 2 do not provide evidence that $\lambda_z$ decreases with increasing altitude. Thus, we conclude that the wavelengths of Arecibo TIDs generally increase with increasing altitude.

Several authors have given the dispersion equation for the full-wave model for thermospheric GW by considering molecular viscosity, thermal diffusivity, and the Coriolis force (e.g., [13]). Ref. [23] considers the wind shear and temperature gradient while neglecting the Coriolis force. Here, we apply the 8th-order polynomial dispersion equation derived in [23] to find the altitudinal variation of the vertical wavelength using the MSIS model atmosphere (assuming no background wind). To obtain the theoretical vertical wavelength, we chose the horizontal wavelength to be 1200 km. The vertical wavelength is plotted in Figure 4c as a black line. The intrinsic wave period is likely different from the observed one. The comparison mainly shows that the observed vertical wavelength is within the realm of theoretical possibilities. We also observe that when dissipations are omitted, the classical isothermal dispersion theory presented in Ref. [30] predicts an increasing vertical wavelength with altitude in the thermosphere. When the temperature gradient is considered, the dispersion relations derived in [23,31] also show the same trend as the isothermal dispersion but at a slower rate. The observed rapid expansion in the vertical wavelength with altitude can only be achieved when dissipations are factored into the model.

One important aspect of TIDs is their often extensive vertical range, spanning several hundred kilometers in altitude. For the driving GWs to propagate over multiple scale heights, the overall dissipation must nearly exactly counterbalance the exponential growth of the wave's amplitude caused by decreasing atmospheric density. If the dissipation is overdamped, the GW will dissipate at lower altitudes. If the dissipation is underdamped, the exponential growth cannot be sustained until the wave breaks. Thus, a suitable thermospheric wave propagation theory needs to have the amplitude-damping term $e^{-0.5z/H}$ as the dominant altitudinal variation term. Only such an amplitude-damping term can account for the largely altitude-invariant $A(\Delta V_z)$, and to a lesser extent, $A(\Delta T_i/T_i)$, as shown in Figure 4a.

## 4. Summary and Conclusions

Simultaneous observations of $N_e$, $V_z$, $T_e$, and $T_i$ using the Arecibo ISR reveal a TID with a period of 135 minutes across all four state variables from 200 to 500 km. The bandpass amplitude of $\Delta N_e/N_e$ within the period from 108 to 180 min, $A(\Delta N_e/N_e)$, reaches a maximum of 16% slightly below the peak F-region altitude. $A(\Delta T_e/T_e)$ is half of $A(\Delta N_e/N_e)$ above 300 km. While $A(\Delta N_e/N_e)$ and $A(\Delta T_e/T_e)$ depend strongly on $N_e$, $A(\Delta V_z)$ and $A(\Delta T_i/T_i)$ have little altitudinal variation, with the former being about 10 m/s and the latter slightly below 2% throughout the altitude range of 200 to 500 km. $\Delta V_z$, $\Delta T_i/T_i$, and $\Delta T_e/T_e$ are mostly in phase, and they are out of phase with $\Delta N_e/N_e$. The vertical wavelength of $\Delta V_z$, $\lambda_z(\Delta V_z)$ increases from 200 km to over 1000 km exponentially in the altitude range of 200–500 km. At geomagnetic mid-latitudes, $\lambda_z(\Delta V_z)$ is a good representation of the GW's vertical wavelength. $A(\Delta T_e/T_e)$ at Arecibo demonstrates stronger altitudinal variation than at EISCAT. At EISCAT, $\lambda_z(\Delta T_e/T_e)$ below 350 km is much larger than those of the other state variables, while the vertical wavelengths of all the variables are about the same at Arecibo.

A major contributor to TIDs in the middle geomagnetic latitude is the GW's meridional velocity. Ion-neutral coupling maps half of a GW's meridional velocity into the vertical direction when the dip angle is 45°. The large vertical ion velocity causes significant fluctuations in electron density through vertical transport. Large electron density variations cause large electron temperature changes as the two variables are closely coupled through the energy balance equation. The meridional-to-vertical velocity coupling explains the ubiquitous presence of TIDs and their preferred equatorward propagation direction at mid-latitudes. The same mechanism also explains the midnight collapse at Arecibo. The fact that $A(\Delta V_z)$ can be observed over several hundred kilometers in altitude without much variation implies that dissipations dampen GW amplitude predominantly in the form of $e^{-0.5z/H}$.

**Author Contributions:** Conceptualization, Q.Z.; methodology, Q.Z. and Y.L.; software, Y.L., Q.Z., and Y.G.; validation, Y.L., Y.G., and Q.Z.; formal analysis, Q.Z.; investigation, Q.Z. and Y.G.; resources, Q.Z.; data curation, Y.L., Q.Z., and Y.G.; writing—original draft preparation, Q.Z.; writing—review and editing, Y.G., Q.Z., and Y.L.; visualization, Q.Z.; supervision, Q.Z.; project administration, Q.Z.; funding acquisition, Q.Z. All authors have read and agreed to the published version of the manuscript.

**Funding:** Y.L. and Q.Z. are supported by the U.S. NSF grant AGS-2152109. G.Y. is supported by the National Natural Science Foundation of China (42374192).

**Data Availability Statement:** The raw data are available at the Texas Advanced Computing Center (https://tacc.utexas.edu/research/tacc-research/arecibo-observatory/). The processed data can be accessed at https://doi.org/10.5281/zenodo.12509945.

**Acknowledgments:** The authors thank the former staff members of the Arecibo Observatory for taking the raw data used in the study.

**Conflicts of Interest:** The authors declare no conflicts of interest.

## References

1. Hocke, K.; Schlegel, K. A review of atmospheric gravity waves and traveling ionospheric disturbances: 1982–1995. *Ann. Geophys.* **1996**, *14*, 917–940.
2. Djuth, F.T.; Sulzer, M.P.; Elder, J.H.; Wickwar, V.B. High resolution studies of atmosphere-ionosphere coupling at Arecibo Observatory, Puerto Rico. *Radio Sci.* **1997**, *32*, 2321–2344.
3. Oliver, W.L.; Otsuka, Y.; Sato, M.; Takami, T.; Fukao, S. A climatology of F region gravity wave propagation over the middle and upper atmosphere radar. *J. Geophys. Res.* **1997**, *102*, 14499–14512.
4. Kumar, S.; Mandal, S.; Pallamraju, D. Characterization of gravity waves in three dimensions in the daytime thermosphere using combined optical and radio measurements and estimation of horizontal neutral winds. *J. Geophys. Res. Space Phys.* **2023**, *128*, e2022JA030954. http://doi.org/10.1029/2022JA030954.
5. Cherniak, L.; Zakharenkova, I. Large-Scale Traveling Ionospheric Disturbances Origin and Propagation: Case Study of the December 2015 Geomagnetic Storm. *Space Weather* **2018**, *16*, 1377–1395. http://doi.org/10.1029/2018SW001869.
6. Djuth, F.T.; Sulzer, M.P.; González, S.A.; Mathews, J.D.; Elder, J.H.; Walterscheid, R.L. A continuum of gravity waves in the Arecibo thermosphere? *Geophys. Res. Lett.* **2004**, *31*, L16801. http://doi.org/10.1029/2003GL019376.
7. Livneh, D.J.; Seker, I.; Djuth, F.; Mathews, J. Continuous quasiperiodic thermospheric waves over Arecibo. *J. Geophys. Res.* **2007**, *112*, A07313. http://doi.org/10.1029/2006JA012225.
8. Zhou, Q. Incoherent scatter radar measurements of vertical winds in the mesosphere. *Geophys. Res. Lett.* **2000**, *27*, 1803–1806.

9. Hysell, D.L.; Larsen, M.F.; Sulzer, M.P. High time and height resolution neutral wind profile measurements across the mesosphere/lower thermosphere region using the Arecibo incoherent scatter radar. *J. Geophys. Res. Space Phys.* **2014**, *119*, 2345–2358. http://doi.org/10.1002/2013JA019621.
10. Nicolls, M.J.; Vadas, S.L.; Aponte, N.; Sulzer, M.P. Horizontal parameters of daytime thermospheric gravity waves and E region neutral winds over Puerto Rico. *J. Geophys. Res. Space Phys.* **2014**, *119*, 575–600. http://doi.org/10.1002/2013JA018988.
11. Li, Y.; Zhou, Q. Measurements of F1- region ionosphere state variables at Arecibo through quasi height-independent exhaustive fittings of the incoherent scatter ion-line spectra. *J. Geophys. Res. Space Phys.* 2024, *submitted*.
12. Kirchengast, G. Elucidation of the physics of the gravity wave-TID relationship with the aid of theoretical simulations. *J. Geophys. Res.* **1996**, *101*, 13353–13368.
13. Hickey, M.P.; Cole, K.D. A quartic dispersion equation for internal gravity waves in the thermosphere. *J. Atmos. Terr. Phys.* **1987**, *49*, 889–899.
14. Zhang, S.D.; Yi, F. A numerical study of propagation characteristics of gravity wave packets propagating in a dissipative atmosphere. *J. Geophys. Res.* **2002**, *107*, 4222. http://doi.org/10.1029/2001JD000864.
15. Vadas, S.L.; Fritts, D.C. Thermospheric responses to gravity waves: Influences of increasing viscosity and thermal diffusivity. *J. Geophys. Res.* **2005**, *110*, D15103. http://doi.org/10.1029/2004JD005574.
16. Knight, H.K.; Broutman, D.; Eckermann, S. A causality-preserving Fourier method for gravity waves in a viscous, thermally diffusive, and vertically varying atmosphere. *Wave Motion* **2019**, *88*, 226–256. http://doi.org/10.1016/j.wavemoti.2019.06.001.
17. Hickey, M.P.; Walterscheid, R.L.; Taylor, M.J.; Ward, W.; Schubert, G.; Zhou, Q.; Garcia, F.; Kelley, M.C.; Shepherd, G.G. Numerical simulations of gravity waves imaged over Arecibo during the 10-day January 1993 campaign. *J. Geophys. Res.* **1997**, *102*, 11475–11489. http://doi.org/10.1029/97JA00181.
18. Walterscheid, R.L.; Hickey, M.P. Group velocity and energy flux in the thermosphere: Limits on the validity of group velocity in a viscous atmosphere. *J. Geophys. Res.* **2011**, *116*, D12101. http://doi.org/10.1029/2010JD014987.
19. Vadas, S.L.; Nicolls, M.J. The phases and amplitudes of gravity waves propagating and dissipating in the thermosphere: Theory. *J. Geophys. Res.* **2012**, *117*. http://doi.org/10.1029/2011JA017426.
20. Zhou, Q.; Li, Y.; Y., G. Variance estimations in the presence of intermittent interference and their applications to incoherent scatter radar signal processing. *Atmos. Meas. Tech.* **2024**, *17*, 4197–4209. http://doi.org/10.5194/amt-17-4197-2024.
21. Djuth, F.T.; Zhang, L.D.; Livneh, D.J.; Seker, I.; Smith, S.M.; Sulzer, M.P.; Mathews, J.D.; Walterscheid, R.L. Arecibo's thermospheric gravity waves and the case for an ocean source. *J. Geophys. Res.* **2010**, *115*, A08305. http://doi.org/10.1029/2009JA014799.
22. Zhou, Q.; Sulzer, M.P. Incoherent scatter radar observation of the F-region ionosphere at Arecibo during January 1993. *J. Atmos. Sol.-Terr. Phys.* **1997**, *59*, 2213–2229.
23. Ma, J.Z.G. Atmospheric Layers in Response to the Propagation of Gravity Waves under Nonisothermal, Wind-shear, and Dissipative Conditions. *J. Mar. Sci. Eng.* **2016**, *4*, 25. http://doi.org/10.3390/jmse4010025.
24. Cho, K.; Marubashi, K.; Kim, R.; Park, S.; Lim, E.; Kim, S.; Kumar, P.; Yurchyshyn, V.; Moon, Y.; Lee, J. Impact of the ICME-Earth Geometry on the Strength of the Associated Geomagnetic Storm: The September 2014 and March 2015 Events. *J. Korean Astron. Soc.* **2017**, *50*, 29–39. http://doi.org/10.5303/jkas.2017.50.2.29.
25. Gong, Y.; Zhou, Q.; Zhang, S. Atmospheric TIDes in the low latitude E- and F- region and their response to a sudden stratospheric warming event in January 2010. *J. Geophys. Res. Space Phys.* **2013**, *118*, 7913–7927. http://doi.org/10.1002/2013JA01924.
26. Francis, S.H. Acoustic-gravity modes and large-scale traveling ionospheric disturbances of a realistic, dissipative atmosphere. *J. Geophys. Res.* **1973**, *78*, 2278–2301.
27. Gong, Y.; Zhou, Q.; Zhang, S.; Aponte, N.; Sulzer, M.; Gonzalez, S. Midnight ionosphere collapse at Arecibo and its relationship to the neutral wind, electric field, and ambipolar diffusion. *J. Geophys. Res. Space Phys.* **2012**, *117*, A08332. http://doi.org/10.1029/2012JA017530.
28. Hocke, K.; Schlegel, K.; Kirchengast, G. Phases and amplitudes of TIDs in the high latitude F region observed by EISCAT. *J. Atmos. Terr. Phys.* **1996**, *58*, 245–255.
29. Vadas, S.L.; Nicolls, M.J. Temporal evolution of neutral, thermospheric winds and plasma response using PFISR measurements of gravity waves. *J. Atmos. Sol.-Terr. Phys.* **2009**, *71*, 740–770.
30. Hines, C.O. Internal atmospheric gravity waves at ionospheric heights. *Can. J. Phys.* **1960**, *38*, 1441–1481.
31. Zhou, Q.; Morton, Y.T. Gravity wave propagation in a non-isothermal atmosphere with height varying background wind. *Geophys. Res. Lett.* **2007**, *34*, L23803. http://doi.org/10.1029/2007GL031061.